AIAA Guidance, Navigation, and Control Conference
13 - 16 August 2012, Minneapolis, Minnesota

AIAA 2012-4814

Sensor-to-Sensor Identification for the SOFIA Testbed

Khaled Aljanaideh *, Benjamin J. Coffer †, Daniel S. Dionne ‡,
Sunil L. Kukreja §, and Dennis S. Bernstein¶

University of Michigan, 1320 Beal Ave., Ann Arbor, MI 48109

In many system identification applications, only output measurements are available for constructing empirical models. In these cases, sensor-to-sensor identification (S2SID) can be used. In the SISO case, one measurement is designated as the pseudo-input, while another measurement is designated as the pseudo-output. Identification between the pseudo-input and pseudo-output results in the construction of a pseudo transfer function (PTF). In the present paper we apply S2SID to data obtained from the NASA SOFIA (Stratospheric Observatory for Infrared Astronomy) testbed. The objective of this work is to determine whether linear PTF models can approximate the relationship between different sensor measurements. The identification of such models can potentially be used in practice to detect faults or changes in a structure.

I. Introduction

In traditional system identification, measurements of input and output signals are used to fit a model of a chosen structure and dynamic order. While system identification techniques are extensively developed [1], there is continued interest in problems such as experiment design, model structure determination, and fit accuracy in the presence of noise. Nonlinear system identification, which may involve gray-box, white box, or black-box model structures, remains a challenging problem with many open and active research directions [2, 3].

In some applications, the input signal may be unknown, and thus sensor measurements are the only available data. If a statistical description of the unknown input is available, then sensor-only identification techniques can be used to detect changes in the dynamics of the system [4–7]. For structural dynamics applications, sensor-only identification is known as operational modal analysis (OMA) [8–10].

In applications where the excitation is unknown and only sensor measurements are available, system identification can be performed by designating one measurement as the pseudo-input and another measurement as the pseudo-output. The identified model, called a pseudo-transfer function, typically captures information about only the zeros, with transmissibility a special case within the context of structural dynamics. Although pole locations are generally not estimated, sensor-to-sensor identification (S2SID) has the advantage of not requiring knowledge of the system excitation. In fact, the unknown ambient system excitation plays the valuable role of providing an excitation that can be used to identify PTFs within S2SID. As one potential application, S2SID is used in [11, 12] to detect system changes. It is essential, however, to ensure that the identified PTF is independent of the excitation signal.

*Graduate Student, Aerospace Engineering Department
†Graduate Student, Aerospace Engineering Department
‡Graduate Student, Aerospace Engineering Department
§Aerospace Engineer, Structural Dynamics Group, NASA Dryden Flight Research Center
¶Professor, Aerospace Engineering Department

A difficulty associated with S2SID is the fact that sensor measurements are not causally related. Consequently, special care is needed to analyze the role of the initial conditions of the underlying input-output system since the underlying state is suppressed in the PTF due to cancellation of the modal dynamics. This issue is analyzed in detail in [12]. Extensions to MIMO PTF identification, which is necessitated by non-scalar excitation, is considered in [13].

In the present paper we apply PTF identification to data measured from the NASA SOFIA (Stratospheric Observatory for Infrared Astronomy) testbed [18]. This data measures vibration response during flight. Since no data are available concerning the excitation forcing, we apply S2SID in order to identify PTFs. The long-range goal of this research is to apply S2SID in order to determine whether S2SID is able to identify PTFs with sufficient accuracy to determine changes in the system.

The contents of the paper are as follows. In Section II we analyze the data set by applying various tests and preprocessing procedures. First, we determine the effective bit count of each signal, which determines the effect of quantization on each signal relative to its range. Next, we compute the coherence function for various signal pairs. We then detrend each signal by removing linear trends, and finally, reanalyze the data sets in terms of the coherence function.

In Section III we describe the PTF models that are fit using least squares. These model structures include time series models as well as μ-Markov models, that is, time series models with explicit Markov parameters [16], [14]. In addition, we fit FIR models indirectly by truncating μ-Markov models and directly by applying least squares with poles constrained to be zero. We briefly review MIMO PTF identification as well as the use of the eigensystem realization algorithm (ERA) for constructing reduced-order models based on the singular value decomposition of the Hankel matrix of Markov parameters [15, 19, 20].

In Section IV we apply the techniques described in Section III to the NASA SOFIA data. In particular, we choose various signal pairs that represent a range of signal quality. For each pair of signals, we consider the effect of detrending on the fits obtained by the methods described in Section III. Fit accuracy is determined by two methods, namely, by applying the pseudo-input data to the identified model (prediction error analysis) and by using both the pseudo-input and pseudo-output data with the identified model for one-step-ahead prediction. The latter method is required when the identified model is unstable, which may arise due to nonminimum-phase zeros in the plant.

In Section V we apply the techniques described in Section III to a simulated mass-spring-damper system. This allows us to explain the phenomena seen with the SOFIA data.

II. Data Analysis and Preprocessing

We apply S2SID to flight data obtained from the SOFIA aircraft located at the NASA Dryden Flight Research Center. The SOFIA aircraft is a highly modified Boeing 747SP, housing an infrared telescope in the aft fuselage. The telescope is isolated from the onboard scientific staff and equipment by means of a pressure dome, thus allowing a door to open for astronomical observations. Due to flight durations of 10 hours or more and the stress of opening the telescope door in-flight, structural health monitoring of both the aircraft and telescope are of great concern. As such, accelerometers have been placed at various locations throughout the aircraft to provide data for post-flight stress analysis.

Experimental flight data was gathered during routine flight at 12,192–15,240 m (40,000–50,000 ft). Data was collected by the accelerometers under ambient conditions during flight. The accelerometer data used in this study was collected from sensors located at the right horizontal stabilizer tip, rear spar (vertical direction), and vertical stabilizer front and rear spars (lateral direction). The sensor data was recorded at 5 kHz and filtered by a sixth-order antialiasing Butterworth filter with a cut-off at 1 kHz. Data was collected while the aircraft operated in a Mach number range from $M = 0.4$–0.7 and dynamic pressures $Q = 26$–390

psf (pounds per square foot). Data was preprocessed to remove the linear trend, mean, and outliers. This ensures that all unwanted low-frequency disturbances, offsets, trends, and drifts are removed. The goal of preprocessing is to minimize the effect of each source of error on the identification. Coherence between signals is studied with and without preprocessing. We later perform S2SID with and without preprocessing in order to ascertain the effects of these procedures.

We begin by estimating how much error exists in the data due to the sensor resolution. In particular, the output resolution is the smallest possible distance between signal measurements. Dividing the output range by the output resolution gives the dynamic range, which is the maximum number of unique sensor output values over the output range. The dynamic range can be expressed in effective bits by finding the base-2 logarithm of the dynamic range. The results of this study are shown in Table 1.

If the coherence between two signals is near unity, then the system is linear, and identification with a linear model structure is justified. In this study, the coherence between most signal pairs is found to degrade at high frequencies. The signal pairs with the best coherence are from sensors located on the same aircraft component. For example, the coherence between two sensors located on the vertical stabilizer is shown in Figure 1(a), while the coherence between a sensor located on the vertical stabilizer and a sensor located on the right horizontal stabilizer is shown in Figure 1(b). Note that the coherence between the sensors located on the vertical stabilizer is better. Therefore, for contrast, identification will be done using sensors that are located near each other, as well as sensor pairs that are distant.

Coherence was checked again after detrending each signal. The best least-squares-fit linear trend was removed from each signal, resulting in zero-mean data. In the most extreme case, the slope of the trend line was 0.038. In most cases the trend line was nearly horizontal, and detrending the signal resulted in only a uniform shift of the signal so that the mean is zero. For these cases, detrending had no effect on the coherence of the signals, as shown in Figure 2. Since detrending has no effect on the coherence, it is not expected to have an effect on the identified model.

NASA Dryden Flight Research Center Photo Collection
http://www.dfrc.nasa.gov/Gallery/Photo/index.html
NASA Photo: ED07–0100–09 Date: May 10, 2007 Photo By: Jim Ross

NASA's Boeing 747SP SOFIA airborne observatory soars over a bed of puffy clouds during its second checkout flight over the Texas countryside on May 10, 2007.

III. Problem Formulation and Identification Methods

A. μ-Markov Model and Least Squares

The linear system shown in Figure 3 has the scalar input u and scalar outputs y_1 and y_2. As shown in Figure 4, we estimate a linear model whose input and output are the signals y_1 and y_2, respectively. This linear model, called a pseudo-transfer-function (PTF), has the form

$$A(\mathbf{q})y_2(k) = B(\mathbf{q})y_1(k), \tag{1}$$

where $\mathbf{q}$ is the forward shift operator, A and B are polynomials in $\mathbf{q}$, and the degree of A is the unknown PTF order n.

For all $k \geq 0$, $\mu \geq 1$, and each model order $n_{\text{mod}} \geq n$, the pseudo-input $y_1(k)$ and pseudo-output $y_2(k)$

Table 1. Sensor Quantization Analysis and Location

Signal	Output Range (m/s^2)	Output Resolution (m/s^2)	Bins	Effective Bits	Location
AC01	21.001	0.0261	805	9.653	Left hand horizontal stabilizer tip front spar, vertical direction
AC02	6.897	0.0257	268	8.066	Left hand horizontal stabilizer tip rear spar, vertical direction
AC03	16.891	0.0261	647	9.338	Right hand horizontal stabilizer tip front spar, vertical direction
AC04	28.632	0.0270	1138	10.152	Right hand horizontal stabilizer tip rear spar, vertical direction
AC05	4.619	0.0259	171	7.418	Vertical stabilizer front spar, lateral direction
AC06	4.608	0.0251	178	7.476	Vertical stabilizer rear spar, lateral direction
AC07	4.717	0.0259	188	7.555	Left hand wing tip, front spar, lateral direction
AC08	5.549	0.0268	214	7.741	Left hand wing tip, rear spar, lateral direction
AC09	5.582	0.0260	208	7.700	Right hand wing tip, front spar, lateral direction
AC10	4.417	0.0250	170	7.409	Right hand wing tip, rear spar, lateral direction
AC103	0.476	0.0251	19	4.248	Aperture acceleration
AC104	0.752	0.0251	30	4.907	Aperture acceleration
AC105	1.579	0.0251	63	5.977	Aperture acceleration
AC106	1.027	0.0251	41	5.358	Aperture acceleration
AC107	0.526	0.0251	21	4.392	Lower flexible door acceleration
AC108	0.927	0.0251	37	5.209	Rear flexible door acceleration

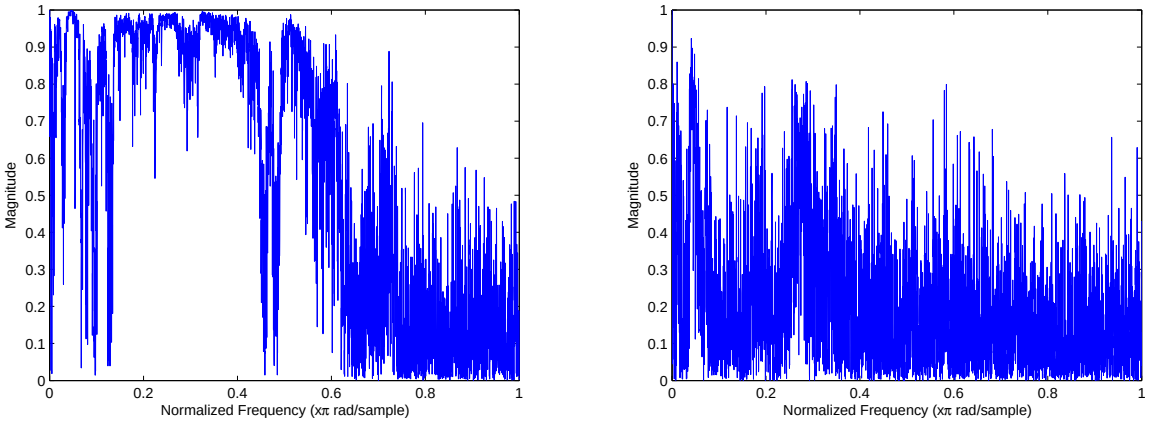

(a) Coherence between sensors AC05 and AC06

(b) Coherence between sensors AC04 and AC05

Figure 1. Example: coherences between signals.

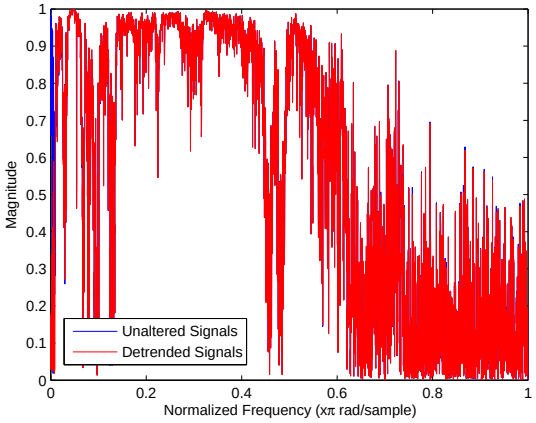

Figure 2. Coherence between signals AC05 and AC06 before and after detrending

satisfy the μ-Markov model

$$y_2(k) = \sum_{j=0}^{\mu-1} H_j y_1(k-j) + \sum_{j=\mu}^{n_{\mathrm{mod}}+\mu-1} b_j y_1(k-j) - \sum_{j=\mu}^{n_{\mathrm{mod}}+\mu-1} a_j y_2(k-j), \tag{2}$$

where $H_0, \ldots, H_{\mu-1}$ are Markov parameters of the PTF, that is, if the outputs $y_2(k-j)$ for all $j \in \{\mu, \ldots, n_{\mathrm{mod}} + \mu - 1\}$ are zero and the input is the impulse $y_1(0) = 1, y_1(k) = 0$ for all $k > 0$, then the first μ outputs of both (1) and (2) are the Markov parameters $H_1, \ldots, H_\mu$ of the PTF. Models of the form (2) are of interest because consistent estimation of $H_1, \ldots, H_\mu$ is possible in the presence of arbitrary output noise using standard least squares [14, 16] when the input y_1 is white. Even though the input to the PTF is not white, we nevertheless use this approach as a convenient technique for estimating Markov parameters.

The μ-Markov model (2) can be expressed as

$$y_2(k) = \theta_\mu \phi_\mu(k) + \theta_{y_1} \phi_{y_1}(k) - \theta_{y_2} \phi_{y_2}(k), \tag{3}$$

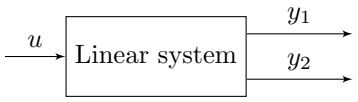

Figure 3. The signal u is the unknown input of the linear system, and y_1 and y_2 are the measured outputs of the linear system.

Figure 4. Definition of the PTF. The PTF is a linear system whose input and output are the linear system outputs y_1 and y_2, respectively. These signals are the pseudo-input and pseudo-output, respectively.

where

$$\begin{aligned}
\theta_\mu &\triangleq \left[\begin{array}{ccc} H_0 & \cdots & H_{\mu-1} \end{array}\right], \\
\theta_{y_1} &\triangleq \left[\begin{array}{ccc} b_\mu & \cdots & b_{n_{\mathrm{mod}}+\mu-1} \end{array}\right], \\
\theta_{y_2} &\triangleq \left[\begin{array}{ccc} a_\mu & \cdots & a_{n_{\mathrm{mod}}+\mu-1} \end{array}\right], \\
\phi_\mu(k) &\triangleq \left[\begin{array}{ccc} y_1(k) & \cdots & y_1(k-\mu+1) \end{array}\right]^{\mathrm{T}}, \\
\phi_{y_1}(k) &\triangleq \left[\begin{array}{ccc} y_1(k-\mu) & \cdots & y_1(k-n_{\mathrm{mod}}-\mu+1) \end{array}\right]^{\mathrm{T}}, \\
\phi_{y_2}(k) &\triangleq \left[\begin{array}{ccc} y_2(k-\mu) & \cdots & y_2(k-n_{\mathrm{mod}}-\mu+1) \end{array}\right]^{\mathrm{T}}.
\end{aligned}$$

Least squares estimates $\hat{\theta}_{\mu,\ell}$, $\hat{\theta}_{y_1,\ell}$, $\hat{\theta}_{y_2,\ell}$ of θ_μ, θ_{y_1}, θ_{y_2} are given by

$$\left[\begin{array}{ccc} \hat{\theta}_{\mu,\ell} & \hat{\theta}_{y_1,\ell} & \hat{\theta}_{y_2,\ell} \end{array}\right] = \underset{\left[\begin{array}{ccc} \bar{\theta}_\mu & \bar{\theta}_{y_1} & \bar{\theta}_{y_2} \end{array}\right]}{\operatorname{argmin}} \left\| \Psi_{y_2,\ell} - \bar{\theta}_\mu \Phi_{\mu,\ell} - \bar{\theta}_{y_1} \Phi_{y_1,\ell} + \bar{\theta}_{y_2} \Phi_{y_2,\ell} \right\|_{\mathrm{F}}, \tag{4}$$

where $\bar{\theta}_\mu, \bar{\theta}_{y_1}, \bar{\theta}_{y_2}$ are variables of appropriate size, $||\,.\,||_{\mathrm{F}}$ denotes the Frobenius norm,

$$\begin{aligned}
\Psi_{y_2,\ell} &\triangleq \left[\begin{array}{ccc} y_2(n_{\mathrm{mod}}+\mu-1) & \cdots & y_2(\ell) \end{array}\right], \\
\Phi_{\mu,\ell} &\triangleq \left[\begin{array}{ccc} \phi_\mu(n_{\mathrm{mod}}+\mu-1) & \cdots & \phi_\mu(\ell) \end{array}\right], \\
\Phi_{y_1,\ell} &\triangleq \left[\begin{array}{ccc} \phi_{y_1}(n_{\mathrm{mod}}+\mu-1) & \cdots & \phi_{y_1}(\ell) \end{array}\right], \\
\Phi_{y_2,\ell} &\triangleq \left[\begin{array}{ccc} \phi_{y_2}(n_{\mathrm{mod}}+\mu-1) & \cdots & \phi_{y_2}(\ell) \end{array}\right],
\end{aligned}$$

and ℓ is the number of samples.

B. PTF Identification Methods

We now describe several techniques for identifying PTF models.

a) **Infinite Impulse Response (IIR)**: We set $\mu = 1$ in (2) and apply the least squares algorithm described above to estimate θ_{y_1} and θ_{y_2}. Equation (4) becomes

$$\left[\begin{array}{cc} \hat{\theta}_{y_1,\ell} & \hat{\theta}_{y_2,\ell} \end{array}\right] = \underset{\left[\begin{array}{cc} \bar{\theta}_{y_1} & \bar{\theta}_{y_2} \end{array}\right]}{\operatorname{argmin}} \left\| \Psi_{y_2,\ell} - \bar{\theta}_{y_1} \Phi_{y_1,\ell} + \bar{\theta}_{y_2} \Phi_{y_2,\ell} \right\|_{\mathrm{F}}. \tag{5}$$

This technique can be applied for a range of values of the model order n_{mod}.

b) **Indirect Finite Impulse Response (IFIR)**: We solve (4) but retain only $\hat{\theta}_{\mu,\ell}$. The output of the resulting FIR PTF model is thus calculated as the convolution between the pseudo-input signal and the Markov parameters identified, that is,

$$y_2(k) = \sum_{j=0}^{\mu-1} H_j y_1(k-j). \tag{6}$$

c) **Direct Finite Impulse Response (DFIR)**: In this case we set θ_{y_1} and θ_{y_2} in (3) to zero and optimize over θ_μ only. The output y_2 is described as

$$y_2(k) = \sum_{j=0}^{\mu-1} H'_j y_1(k-j). \tag{7}$$

We define

$$\theta'_\mu \triangleq \begin{bmatrix} H'_0 & \cdots & H'_{\mu-1} \end{bmatrix}, \tag{8}$$

where θ'_μ is estimated using the optimization

$$\hat{\theta}'_{\mu,\ell} = \underset{[\,\bar{\theta}'_\mu\,]}{\operatorname{argmin}} \left\| \Psi_{y_2,\ell} - \bar{\theta}'_\mu \Phi_{y_1,\ell} \right\|_{\mathrm{F}}. \tag{9}$$

d) **Eigensystem Realization Algorithm (ERA)**: The ERA algorithm constructs an IIR model by computing the singular value decomposition of the Hankel matrix constructed from the Markov parameters of the system [17]. We estimate the Markov parameters using (4), and then we apply the ERA algorithm to obtain an estimated PTF in state space form.

e) **Multi-Input, Single-Output (MISO) PTFs**: For reasons discussed in [13], we consider up to four inputs and a single output PTF. For example, for the case of two inputs and one output (2ISO), we assume that the PTF has the form shown in Figure 5, and we apply the identification techniques described above to the 2ISO case.

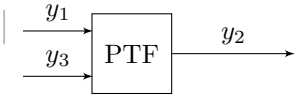

Figure 5. The signals y_1 and y_3 are the inputs and y_2 is the output of the 2ISO PTF.

C. Evaluating the accuracy of identified model

We evaluate the accuracy of the identified models by calculating the prediction error (PE) defined by

$$\varepsilon \triangleq \|y_2 - y'_2\|, \tag{10}$$

where y_2 is the computed PTF output and y'_2 is the pseudo-output data.

In some cases the identified PTF is unstable. This may be a consequence of nonminimum-phase zeros in the transfer function, or it may be a spurious consequence of noise or nonlinearity. To quantify the accuracy of the fit when the identified model is unstable, we use both the pseudo-input data and the pseudo-output data and use the identified model to compute a one-step-ahead prediction. The error in this case is the norm of the difference between the measured pseudo-output and the computed pseudo-output. The computed pseudo-output is not used subsequently in the simulation. We define this error as the *all-data error* (ADE) since both pseudo-input data and pseudo-output data are used to simulate the identified model.

D. Choosing the model order n_{mod}

To estimate the model order, we begin with an initial estimate $\hat{n}$ of n that exceeds the model order n. We set $\mu = 2\hat{n} - 1$ in (4) and obtain the estimated Markov parameters to construct the Markov block-Hankel matrix

$$\mathcal{H}(H) \triangleq \begin{bmatrix} H_1 & \cdots & H_{\hat{n}} \\ \vdots & \ddots & \vdots \\ H_{\hat{n}} & \cdots & H_{2\hat{n}-1} \end{bmatrix}, \tag{11}$$

where H is the vector or matrix of Markov parameters defined as

$$H \triangleq \begin{bmatrix} H_0 & \cdots & H_{2\hat{n}-1} \end{bmatrix}, \tag{12}$$

and $\mathcal{H}(\cdot)$ is a linear mapping that constructs a Markov block-Hankel matrix from the components of the vector H except for H_0. The rank of $\mathcal{H}(H)$ is equal to the McMillan degree of the PTF.

We compute the singular values of $\mathcal{H}(H)$ and look for a large decrease in the singular values. For noise-free data, a large decrease in the singular values is evident. Simulation results show that, even with a small amount of noise, the large decrease in the singular values disappears and thus the problem of estimating the model order becomes difficult. The nuclear-norm minimization technique given in [19, 20] provides a heuristic optimization approach to this problem. In particular, define the optimization parameter vector $\hat{H}$ as

$$\hat{H} \triangleq \begin{bmatrix} \hat{H}_0 & \cdots & \hat{H}_{2\hat{n}-1} \end{bmatrix}. \tag{13}$$

To estimate the model order we solve the optimization problem

$$\underset{\hat{H}}{\text{minimize}} \left\| \mathcal{H}(\hat{H}) \right\|_{\mathrm{N}} \tag{14}$$

$$\text{subject to} \left\| \hat{H} - H \right\|_{\mathrm{F}} \leq \gamma, \tag{15}$$

where $\| \cdot \|_{\mathrm{N}}$ denotes the nuclear norm, and γ is varied from zero to $\|\mathcal{H}(H)\|_{\mathrm{F}}$. For each value of γ, we find the optimal $\hat{H}(\gamma)$, and then we construct the Markov block-Hankel matrix $\mathcal{H}(\hat{H}(\gamma))$ and compute its singular values. We define the ϵ-rank of a matrix to be the number of nonzero singular values after setting all the singular values below ϵ to zero. If, for a relatively wide range of γ, the same ϵ-rank value is obtained, then we consider it to be the McMillan degree of the system of interest.

The following example illustrates this method.

Example III.1. Consider the second-order transfer function

$$G(\mathbf{q}) = \frac{(\mathbf{q} + 0.5)(\mathbf{q} + 0.3)}{(\mathbf{q} - 0.3)(\mathbf{q} - 0.8)}. \tag{16}$$

We use a gaussian input and add input and output noise with signal-to-noise ratio of 10. Let H' and H be vectors of Markov parameters obtained from (4) with noise-free data and data corrupted with noise, respectively. We set $\hat{n} = 20$ and solve the optimization problem (14), (15) for a range of γ from 0 to $\|\mathcal{H}(H)\|_{\mathrm{F}}$. For each value of γ, we find the optimal $\hat{H}(\gamma)$, and then we construct the Markov block-Hankel matrix $\mathcal{H}(\hat{H}(\gamma))$ and compute its singular values. We set $\epsilon = 1 \times 10^{-5}$, that is, all singular values below this threshold are set to zero, which yields the ϵ-rank for each γ. Figure 6 shows a plot of ϵ-rank$(\mathcal{H}(\hat{H}(\gamma)))$ versus γ. We note that, for a relatively large range of γ, we have ϵ-rank$(\mathcal{H}(\hat{H}(\gamma))) = 2$, which is in fact the order of the system. Figure 7 shows the singular values for noise-free data (triangles), data corrupted with noise (circles), and after nuclear norm minimization (NNM) (squares) for $\gamma = 0.313$. This value of γ was chosen from Figure 6 for which ϵ-rank$(\mathcal{H}(\hat{H}(\gamma))) = 2$. Note the relatively large gap after the second singular value after performing nuclear norm minimization.

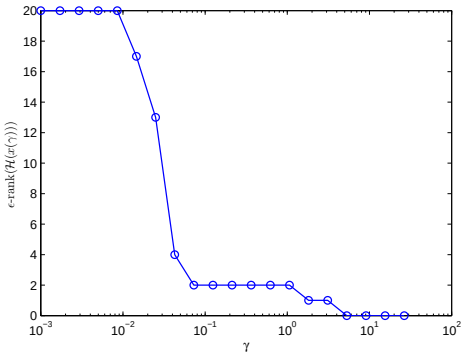

Figure 6. ϵ-rank of $\mathcal{H}(\hat{H}(\gamma))$ versus γ for example III.1, where $\epsilon = 1 \times 10^{-5}$. The plot suggests that the system in (16) is a second-order system.

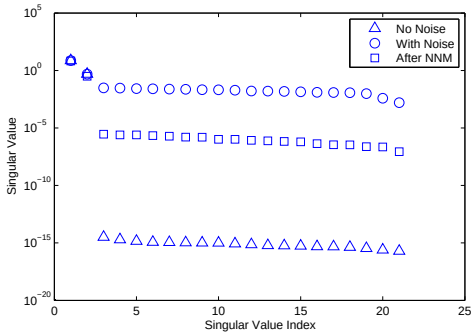

Figure 7. Singular values for $\mathcal{H}(H')$ (triangles), $\mathcal{H}(H)$ (circles), and $\mathcal{H}(\hat{H}(\gamma))$ (squares) for example III.1, when $\gamma = 0.313$. Note the relatively large gap after the second singular value after performing nuclear norm minimization.

IV. Examples with SOFIA Accelerometer Data

In this section, we apply the identification methods described above to the SOFIA accelerometer data. For the first two examples, we consider the following cases:

a) Pseudo-input is AC05 and pseudo-output is AC06.

b) Pseudo-input is AC04 and pseudo-output is AC06.

c) Pseudo-inputs are AC04 and AC05, and pseudo-output is AC06.

Example IV.1. Consider the IIR model. Figure 8 shows PE-versus-n_{mod} plots for the three cases above. Note that, for the IIR model, PE decreases as n_{mod} increases. Also, note that detrending the data reduces the PE in all cases.

Example IV.2. To construct an IIR model, we apply the nuclear norm minimization method to choose the model order n_{mod}. For each case, we choose $\hat{n} = 20$ and set the singular value threshold to $\epsilon = 1 \times 10^{-5}$, where γ is varied from 0.1 to 2. Figures 9, 10, and 11 show plots of ϵ-rank$(\mathcal{H}(\hat{H}(\gamma)))$ versus γ for cases a), b), and c), respectively. Note that the three figures do not give definitive values for the rank due possibly to high levels of noise. However, we choose $n_{\text{mod}} = 2$ for case a), $n_{\text{mod}} = 1$ for case b), and $n_{\text{mod}} = 12$ for case c) since they exhibit the widest range of γ for each case.

Table 2 shows the smallest PE value obtained for the cases above using the identification techniques discussed in the previous section. We note that both IFIR and DFIR achieve the smallest error for cases a) and c). IIR shows poor behavior for all three cases. Case b) identification is the worst of the three cases, which is due to the poor coherence between AC04 and AC06.

Table 2. Identification methods comparison, error calculation is based on PE

	Case a)	Case b)	Case c)
IIR	42.9467	37.8612	39.6049
IFIR	18.4114	38.0624	17.9470
DFIR	18.0532	37.6029	17.4933
ERA	28.1186	41.0648	27.1831

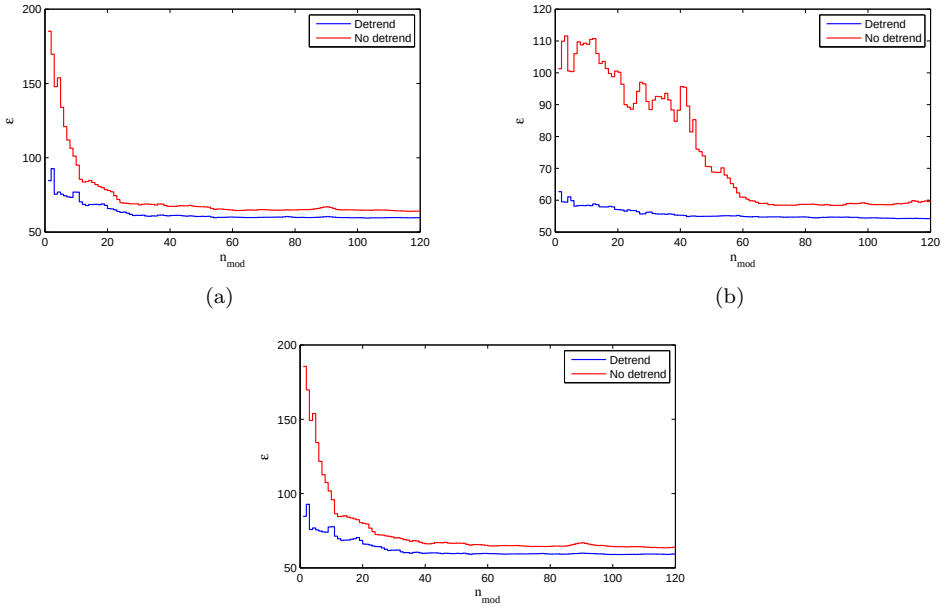

Figure 8. IIR PTF Identification with error ε calculated as PE. (a) Pseudo-input is AC05 and pseudo-output is AC06 (b) Pseudo-input is AC04 and pseudo-output is AC06 (c) Pseudo-inputs are AC04 and AC05, and pseudo-output is AC06.

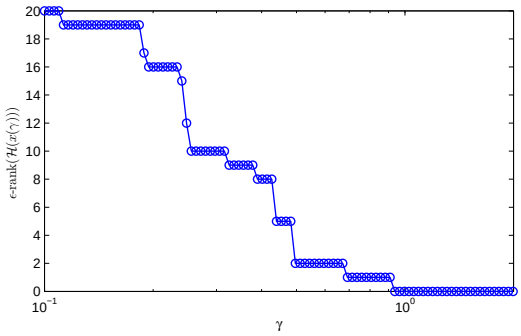

Figure 9. Plot of ϵ-rank of $\mathcal{H}(\hat{H}(\gamma))$ versus γ for case a), where $\epsilon = 1 \times 10^{-5}$. Note that this plot does not give a definitive value for the rank due possibly to high levels of noise. However, $n_{\text{mod}} = 2$ covers the widest range of γ for this case.

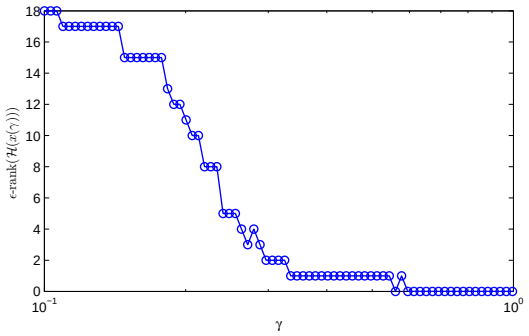

Figure 10. Plot of rank of $\mathcal{H}(\hat{H}(\gamma))$ versus γ for case b), where $\epsilon = 1 \times 10^{-5}$. Note that this plot does not give a definitive value for the rank due possibly to high levels of noise. However, $n_{\text{mod}} = 1$ covers the widest range of γ for this case.

Example IV.3. In this example, we explore MISO FIR ID on a subset of accelerometer signals from the SOFIA aircraft. Seventy-five MISO DFIR models (with $\mu = 300$) are fit to detrended signals AC03, AC04, AC05, AC06, and AC07 for all possible input/output combinations. For each model fit, an error measurement is obtained by dividing the model's PE by the maximum amplitude of the measured PTF output signal. This normalization is performed to facilitate comparisons between models with different output amplitudes.

Tables 3, 4, and 5 summarize the results obtained in this example. Table 3 shows the error for each SISO fit sorted left-to-right by error size. Table 4 shows the best possible SISO and MISO fits (and their corresponding error) for each output and for increasing numbers of inputs. For comparison, Table 5 shows the worst possible fits for the same categories as Table 4. Note that best possible and worst possible are defined in terms of prediction error.

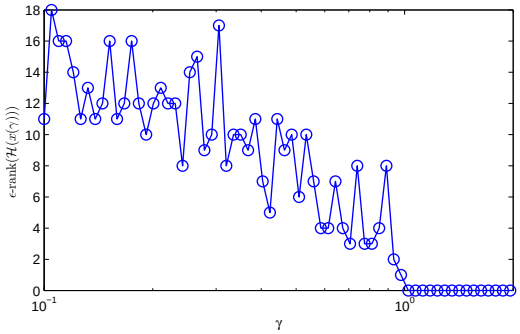

Figure 11. Plot of ϵ-rank of $\mathcal{H}(\hat{H}(\gamma))$ versus γ for case c), where $\epsilon = 1 \times 10^{-3}$. Note that this plot does not give a definitive value for the rank due possibly to large levels of noise. However, we choose $n_{\text{mod}} = 12$ since it covers the widest range of γ for this case.

By examining Tables 3, 4, and 5, the following observations can be made:

i) The best identification results are obtained between accelerometers located near each other.

ii) Adding more inputs may reduce or increase the error.

iii) The best MISO fits have a 4% lower error than the best SISO fits.

iv) For a given output, the best possible collection of m-inputs includes the best possible collection of $(m-1)$-inputs.

v) For a given output, the best possible collection of m-inputs are often the m best SISO inputs.

Figure 12 shows the simulated output of a 2ISO PTF exhibiting a good fit along with the measured data. For comparison, Figure 13 shows the simulated output of a 2ISO PTF exhibiting a poor fit.

Table 3. Error for each SISO fit. The table is sorted left-to-right by error size.

	1 Input	1 Input	1 Input	1 Input
AC03 Output	AC04 (6.33)	AC06 (15.04)	AC05 (15.22)	AC07 (16.38)
AC04 Output	AC03 (9.05)	AC05 (13.28)	AC06 (13.39)	AC07 (13.86)
AC05 Output	AC06 (6.83)	AC04 (14.42)	AC03 (14.71)	AC07 (15.95)
AC06 Output	AC05 (6.85)	AC04 (15.13)	AC03 (15.41)	AC07 (17.05)
AC07 Output	AC05 (17.73)	AC06 (17.99)	AC03 (18.06)	AC04 (18.17)

Table 4. Best possible SISO and MISO fits (and corresponding error) for each category specified by the row and column. For a multi-input model, the inputs consist of the input in the corresponding column and all inputs to its left.

	1 Input	2 Input	3 Input	4 Input
AC03 Output	AC04 (6.33)	and AC06 (6.08)	and AC07 (6.19)	and AC05 (6.42)
AC04 Output	AC03 (9.05)	and AC05 (9.11)	and AC06 (9.10)	and AC07 (9.93)
AC05 Output	AC06 (6.83)	and AC04 (6.72)	and AC03 (6.78)	and AC07 (6.87)
AC06 Output	AC05 (6.85)	and AC04 (6.79)	and AC03 (6.67)	and AC07 (6.87)
AC07 Output	AC05 (17.73)	and AC06 (18.42)	and AC03 (19.26)	and AC04 (20.28)

Table 5. Worst possible SISO and MISO fits (and corresponding error) for each category specified by the row and column. For a multi-input model, the inputs consist of the input in the corresponding column and all inputs to its left.

	1 Input	2 Input	3 Input	4 Input
AC03 Output	AC07 (16.38)	and AC05 (15.69)	and AC06 (15.71)	and AC04 (6.42)
AC04 Output	AC07 (13.86)	and AC06 (13.81)	and AC05 (14.05)	and AC03 (9.93)
AC05 Output	AC07 (15.95)	and AC03 (15.48)	and AC04 (15.48)	and AC06 (6.87)
AC06 Output	AC07 (17.05)	and AC03 (16.24)	and AC04 (16.10)	and AC05 (6.87)
AC07 Output	AC04 (18.17)	and AC03 (19.19)	and AC06 (19.73)	and AC05 (20.28)

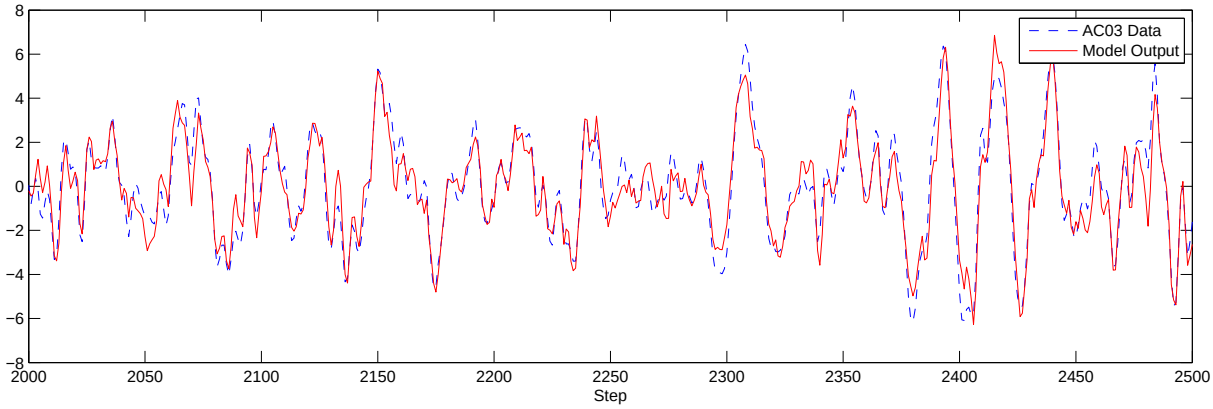

Figure 12. Example of a good fit: AC04 and AC06 input to AC03 output.

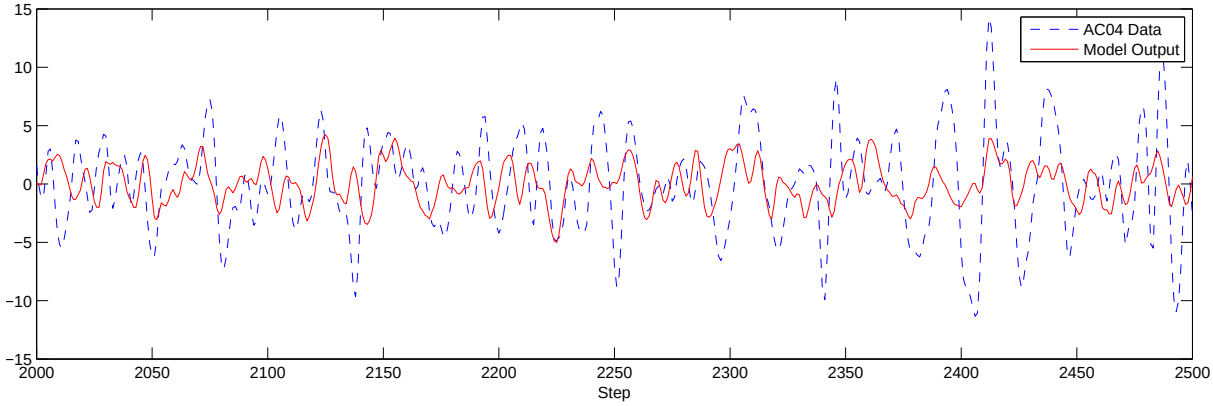

Figure 13. Example of a poor fit: AC06 and AC07 input to AC04 output.

Example IV.4. From Example IV.2 above we find that the most accurate model fits, as determined by PE are obtained from least-squares optimization of FIR time-series models. However, these investigations provided an unexpected feature illustrated in Figure 14. Specifically, Figure 14 shows that the PE decreases as the PTF output signal is delayed relative to the PTF input. The reason for this surprising effect becomes clear upon plotting the impulse response of the identified FIR model. As shown in Figure 15, the impulse response of the FIR model has a significant noncausal component, plotted to the left of the chosen delay. To confirm that the noncausal component of the identified FIR impulse response is contributing to the PE, we remove the noncausal component and then re-include it one impulse parameter at a time; this is done by including the impulse response parameters one at a time from the left of the chosen delay in Figure

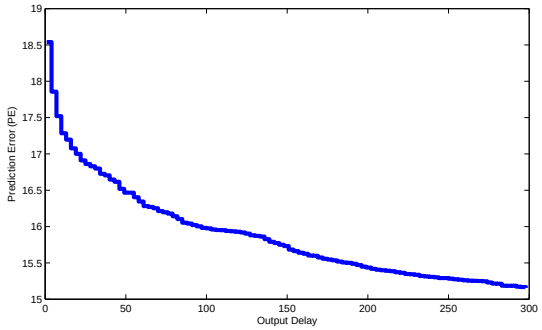

Figure 14. Prediction Error for an identified FIR model using DFIR as a function of output delay. Delaying the output data relative to the input data improves the accuracy of the identified FIR model as measured by the PE criterion.

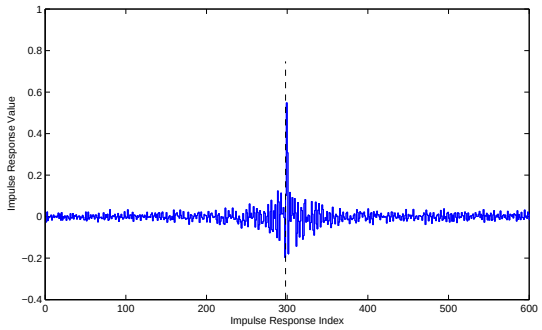

Figure 15. Impulse response of an identified FIR model with a delay of 298 steps applied to the output data. The surprising feature of this impulse response is that it has a significant noncausal component, which appears to the left of the delay of 298 steps.

15. Figure 16 shows that the PE decreases as noncausal impulse response parameters are included in the identified FIR model.

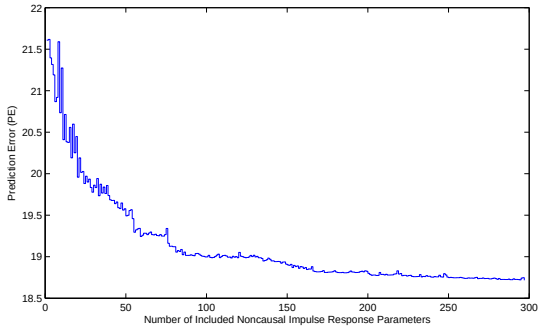

Figure 16. The PE criterion is plotted here as an increasing number of noncausal impulse response parameters are included in the model. This plot confirms that the noncausal component of the estimated model enhances the prediction accuracy.

V. Examples with Simulated Mass-Spring-Damper System

In order to better understand the phenomena seen with the SOFIA data, the identification techniques described in Section III.B are applied to the mass-spring-damper system shown in Figure 17.

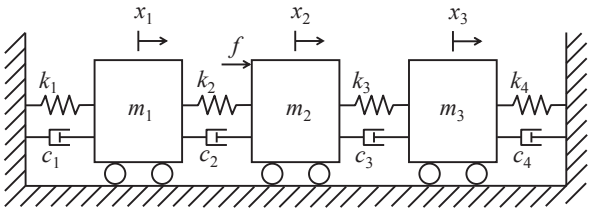

Figure 17. Mass-spring-damper system. This system is used to produce synthetic data for investigating phenomena seen with the SOFIA data. By adjusting the parameters, stable and unstable PTFs can be constructed.

Example V.1. As seen in Example IV.2, FIR models can produce a much smaller PE than IIR models. To investigate this phenomenon, we simulate the mass-spring-damper system shown in Figure 17 with the parameters $m_1 = 4$ kg, $m_2 = 3$ kg, $m_3 = 2$ kg, $k_1 = 99$ N/m, $k_2 = 28$ N/m, $k_3 = 310$ N/m, $k_4 = 101$ N/m, $c_1 = 0.9$ N-s/m, $c_2 = 5.1$ N-s/m, $c_3 = 0.8$ N-s/m, $c_4 = 5.2$ N-s/m, and discretization time step $T_s = 0.2$ s. The system is simulated with a white-noise input force f to obtain the velocities v_1 and v_3 of mass 1 and mass 3, respectively. Several models are then identified for the PTF from v_3 to v_1. These models include IIR models with model orders n between 1 and 8, and FIR models with impulse response lengths μ between 1 and 301. For each model, PE is calculated. These PEs are shown by the circle-markers in Figure 18. The entire example is then repeated, but with output noise (SNR $= 10^8$) added to the simulation. The resulting prediction errors are shown by the x-markers in Figure 18.

Both IIR and FIR models perform equally well provided that n_{mod} and μ are set to a suitable value. However, the IIR fits produced good results only for $n_{\text{mod}} = 4$, whereas the FIR fits produce good results for all sufficiently high μ.

This example reveals a possible explanation for why FIR models perform better than IIR models on the SOFIA data. It is possible that we cannot find the correct model order of the SOFIA PTF's, and therefore we cannot construct an IIR model of the true order n. However, we are able to construct a suitable FIR model because we need only to select a sufficiently large value of μ without specifying n_{mod}.

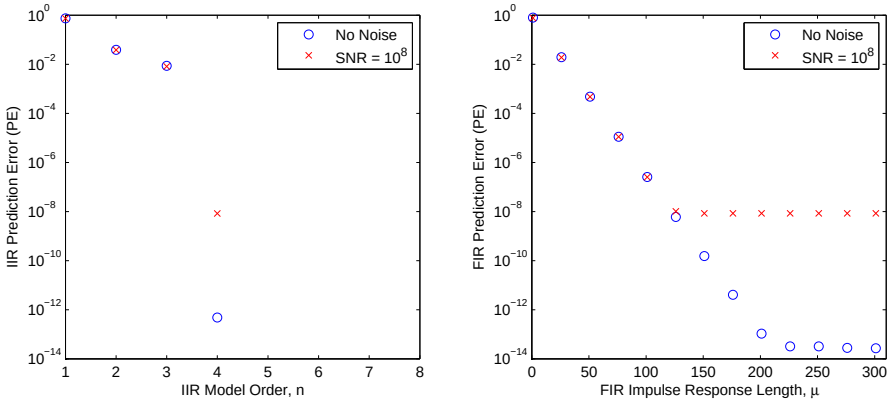

Figure 18. Prediction error of various IIR and FIR models identified from data obtained by simulating the system shown in Figure 17. Prediction errors for IIR models with $n > 4$ are extremely large and are not shown. A low PE is obtained for IIR models with $n = 4$ and for FIR models with sufficiently large μ.

Example V.2. As seen in Example IV.4, the prediction error in FIR models can often be reduced by introducing a delay to the PTF output. This output delay effectively allows the FIR model to be noncausal. To investigate the origin of this property, we again simulate the mass-spring-damper system shown in Figure 17 using the same parameters as Example V.1 and discretization time step $T_s = 0.2$ s. The system is simulated with a white-noise input force f to obtain the velocities v_1 and v_3 of mass 1 and mass 3, respectively. For this system, the PTF from v_3 to v_1 is stable. The v_1 data from the simulation is then delayed by 10 steps, and an FIR model was identified from v_3 to the delayed v_1. The resulting impulse response of the identified FIR model is shown in Figure 19. Note that the first 10 impulse response values are zero. This indicates that the identified FIR model is causal.

The example is then repeated with m_3 set to 20 kg. This causes the PTF from v_3 to v_1 to be unstable. This may seem surprising since the mass-spring-damper system is stable and both signals v_1 and v_3 are bounded. However, the transfer function from f to v_3 in this case is nonminimum phase; that is, it has zeros outside of the unit circle. Therefore, the PTF from v_3 to v_1 is unstable.

The system is simulated with a white-noise input force f to obtain the velocity signals v_1 and v_3. The data v_1 from the simulation is then delayed by 10 steps, and an FIR model is identified from v_3 to the delayed v_1. The resulting impulse response of the identified FIR model is shown in Figure 20. Note that the first 10 impulse response values are nonzero. This indicates that the identified FIR model is noncausal.

This example suggests that the best FIR model of a stable PTF is obtained with a causal FIR model, whereas the best FIR model of an unstable PTF is obtained with a noncausal FIR model. Therefore, a possible explanation for why the PTF's in the SOFIA data are best identified with noncausal FIR models is that at least some of the SOFIA PTF's may be unstable.

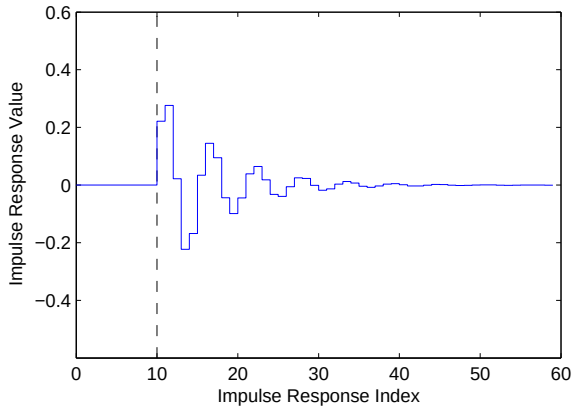

Figure 19. PTF identification is applied to the structure in Figure 17 with the parameters $m_1 = 4$ kg, $m_2 = 3$ kg, $m_3 = 2$ kg, $k_1 = 99$ N/m, $k_2 = 28$ N/m, $k_3 = 310$ N/m, $k_4 = 101$ N/m, $c_1 = 0.9$ N-s/m, $c_2 = 5.1$ N-s/m, $c_3 = 0.8$ N-s/m, $c_4 = 5.2$ N-s/m, and discretization time step $T_s = 0.2$ s. A random white noise force excitation is applied to m_2. The pseudo-input is the velocity of m_3, and the pseudo-output is the velocity of m_1. The estimated PTF impulse response is found to be causal.

VI. Conclusions

In this paper we identified linear SISO and MISO pseudo-transfer functions (PTFs) using data from the NASA SOFIA testbed. Detrending was applied to the signals in order to remove linear trends. We discussed several identification techniques for constructing PTFs, including IIR, direct and indirect FIR, and ERA. We found that FIR gives the best fits. We showed that using multiple inputs may either increase or reduce the error compared to using single-input fits. Finally, we studied the effect of output delay on improving the fits obtained and found that the best FIR fits have a significant noncausal component. We showed using stable

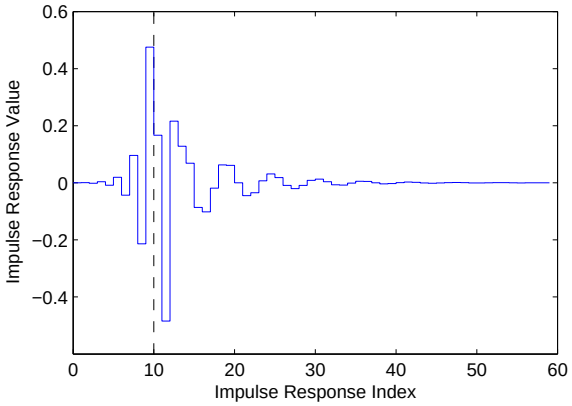

Figure 20. PTF identification is applied to the structure in Figure 17 with the parameters as in Figure 19 except that now $m_3 = 20$ kg. In this case, the estimated impulse response is found to be noncausal. The noncausal component of the impulse response is due to the fact that one of the transfer functions from excitation to measurement is nonminimum phase, and therefore the PTF from the pseudo-input to the pseudo-output is unstable. The instability of the PTF induces a noncausal component in the PTF impulse response.

and unstable PTFs constructed from a lumped mass-spring-damper system that the noncausal component is due to the fact that the identified PTFs are unstable.

References

[1]Ljung, L. (1999) System Identification: Theory for the User, 2nd ed. *Upper Saddle River, NJ*: Prentice-Hall Information and Systems Sciences.

[2]Sjoberg, J. and et al (1995) Nonlinear Black-Box Modeling in System Identification: A Unified Overview *Automatica*, vol. 31, pp. 1691–1724.

[3]Haber, R. and Keviczky, L. (1999) Nonlinear System Identification–Input-Output Modeling Approach Vol. 1: Nonlinear System Parameter Identification *Kluwer Academic Publishers*.

[4]Parloo, E., Vanlanduit, S., Guillaume, P., and Verboven, P. Increased reliability of reference-based damage identification techniques by using output-only data. *J. Sound & Vib.*, vol. 270, pp. 813-832.

[5]Mevel, L., Benveniste, A., Basseville, M., Goursat, M., Peeters, B., Van der Auweraer, H., and Vecchio, A. Input/output versus output only data processing for structural identification–application to in-flight data analysis. *J. Sound & Vib.*, vol. 295, pp. 531-552.

[6]Spiridonakos, M. D., Poulimenos, A. G., and Fassois, S. D. Output-only identification and dynamic analysis of time-varying mechanical structures under random excitation: a comparative assessment of parametric methods. *J. Sound & Vib.*, vol. 329, pp. 768-785.

[7]Basseville, M., Benveniste, A., Goursat, M., Hermans, L., Mevel, L. and Van der Auweraer, H. Output-only subspace-based structural identification: from theory to industrial testing practice *ASME Journal of Dyn. Sys., Meas., & Cont.*, vol. 123, pp. 668-676.

[8]Peeters, B. and De Roeck, G. Stochastic System Identification for Operational Modal Analysis: A Review *ASME Journal of Dyn. Sys., Meas., & Cont.*, vol. 123, pp. 659-667.

[9]Rainieri, C. and Fabbrocino, G. Automated output-only dynamic identification of civil engineering structures *Mech. Sys. & Sig. Proc.*, vol. 24, pp. 678-695.

[10]Devriendt, C. and Guillaume, P. (2008) Identification of modal parameters from transmissibility measurements. *J. Sound & Vib.*, vol. 314, pp. 343–356.

[11]D'Amato, A. M., Brzezinski, A. J., Holzel, M. S., Ni, J., and Bernstein, D. S. (2009). Sensor-only noncausal blind identification of pseudo transfer functions. *Proc. SYSID*, Saint-Malo, France, pp. 1698–1703.

[12]Brzezinski, A. J., Kukreja, S. L., Ni, J., and Bernstein, D. S. (2010). Sensor-only fault detection using pseudo transfer function identification. *Proc. Amer. Conf. Contr.*, Baltimore, MD, pp. 5433–5438.

[13]Brzezinski, A., Kukreja, S., Ni, J., and, Bernstein, D. S. (2011). Identification of Sensor-Only MIMO Pseudo Transfer Functions. *Proc. Conf. Dec. Contr.*, Orlando, FL, pp. 2154–2159.

[14]Kamrunnahar, M., Huang, B., and Fisher, D. B. (1999). Estimation of markov parameters and time-delay/interactor matrix. *Chemical Engineering Science*, pp. 3353–3363.

[15]Juang, J. N. (1993) Applied System Identification. *Upper Saddle River, NJ*: Prentice-Hall, 1993.

[16]Fledderjohn, M. S. and Holzel, M. S., Palanthandalam-Madapusi, H., Fuentes, R. J. and Bernstein, D. S. (2010). A Comparison of Least Squares Algorithms for Estimating Markov Parameters. *Proc. Amer. Contr. Conf.*, Baltimore, MD, pp. 3735–3740.

[17]Juang, J. N., Pappa, R. S. (1985). An Eigensystem Realization Algorithm for Modal Parameter Identification and Model Reduction. *J. of Guidance, Contr. & Dynamics*, vol. 8, no. 5, pp. 620–627.

[18]www.nasa.gov/sofia

[19]Smith, R. (2012). Nuclear Norm Minimization Methods for Frequency Domain Subspace Identification. *Proc. Amer. Conf. Contr.*, Montreal, Canada, pp. 2689–2694.

[20]Recht, B., Fazel, M., and Parrilo, P. A. (2010). Guaranteed Minimum-Rank Solutions of Linear Matrix Equations via Nuclear Norm Minimization. *SIAM Review*, Vol. 52, No. 3, pp. 471-501.